Influence of annealing on microstructure and mechanical properties of ultrafine-grained Ti45Nb

B. Völker [a,1], V. Maier-Kiener [b], K. Werbach [c], T. Müller [a,2], S. Pilz [d], M. Calin [d], J. Eckert [a,e], A. Hohenwarter [e,*]

[a] Erich Schmid Institute of Materials Science, Austrian Academy of Sciences, Jahnstraße 12, 8700 Leoben, Austria
[b] Department of Materials Science, Chair of Physical Metallurgy and Metallic Materials, Montanuniversität Leoben, Roseggerstraße 12, 8700 Leoben, Austria
[c] Faculty of Physics, University of Vienna, Boltzmanngasse 5, A-1090 Vienna, Austria
[d] Leibniz Institute for Solid State and Materials Research Dresden, Helmholtzstr. 20, 01069 Dresden, Germany
[e] Department of Materials Science, Chair of Materials Physics, Montanuniversität Leoben, Jahnstraße 12, 8700 Leoben, Austria

HIGHLIGHTS

- A Ti-45wt.%Nb alloy was processed by means of severe plastic deformation for obtaining a nanocrystalline structure.
- The strength is considerably increased and shows good thermal stability.
- By annealing treatments strength can be even further increased.
- The annealing also leads to a small increase of Young's modulus.
- Annealing leads to formation of a Ti-rich α-phase at grain boundaries.

GRAPHICAL ABSTRACT
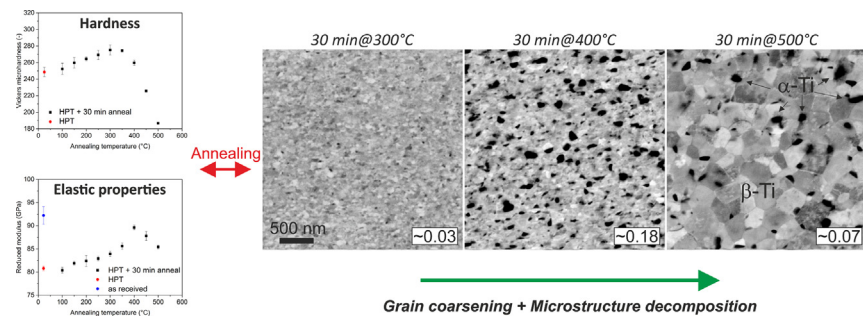
ABSTRACT

Beta-Ti alloys have been intensively investigated in the last years because of their favorable low Young's moduli, biocompatibility and bio-inertness, making these alloys interesting candidates for implant materials. Due to their low mechanical strength, efforts are currently devoted to increasing it. A promising way to improve the strength is to tailor the microstructure using severe plastic deformation (SPD). In this investigation high pressure torsion was used to refine the microstructure of a Ti-45wt.%Nb alloy inducing a grain size of ~50 nm. The main focus of the subsequent investigations was devoted to the thermal stability of the microstructure. Isochronal heat-treatments performed for 30 min in a temperature range up to 500 °C caused an increase of hardness with a peak value at 300 °C before the hardness decreased at higher temperatures. Simultaneously, a distinct temperature-dependent variation of the Young's modulus was also measured. Tensile tests revealed an increase in strength after annealing compared to the SPD-state. Microstructural investigations showed that annealing causes the formation of α-Ti. The findings suggest that the combination of severe plastic deformation with subsequent heat treatment provides a feasible way to improve the mechanical properties of SPD-deformed β-Ti alloys making them suitable for higher strength applications.

* Corresponding author.
  E-mail address: anton.hohenwarter@unileoben.ac.at (A. Hohenwarter).
[1] Now at: Chair of Materials Chemistry, RWTH Aachen, Kopernikusstrasse 10, 52074 Aachen, Germany & Max-Planck-Institut für Eisenforschung GmbH, Max-Planck-Straße 1, 40237 Düsseldorf, Germany.
[2] Now at: Deutsches Elektronen-Synchrotron DESY, Photon Science, Notkestraße 85, 22607 Hamburg, Germany.

1. Introduction

The alloy system Ti—Nb has a minimum of the Young's modulus at approximately 45 wt.% Nb making Ti45Nb an interesting β-Ti alloy for medical implants [1–3]. A general drawback of low modulus β-Ti alloys are their inferior mechanical properties [4–6]. Hence, a lot of research aims to increase the mechanical strength of these alloys [7–11]. Work hardening [12–15] may provide a possibility to increase the strength without changing the Young's modulus. Especially methods of severe plastic deformation (SPD) are capable of reducing the grain size down to the sub-micron and nanometer regime in combination with a significant strength increase [16–19]. Among all SPD methods high pressure torsion (HPT) generally leads to the smallest grain sizes especially for difficult to deform materials [20–22]. This can be explained by the high applicable hydrostatic pressures using HPT. It prevents premature failure of the sample during deformation and allows the largest amounts of shear deformation to be imposed on the material. Previous investigations have already demonstrated that HPT deformation of the Ti45Nb alloy leads to a significant increase of strength of the initially coarse-grained material [9,12]. Additionally, it was shown that the fracture toughness of the material remains high [13] compared to other Ti-based materials either used or considered as implant materials for load bearing applications [8,10,23–26].

This study focuses on the annealing behavior and thermal stability of the SPD-processed material. Even though medical implants do not require high thermal stability during their use in the human body, it has significance for other aspects. First, during the machining of the implant from the SPD-deformed pre-material significant temperature rises can occur. Second, annealing treatments of SPD-deformed materials are often used to obtain a better balance between strength and ductility [27]. Third, several studies showed that the annealing of SPD-processed materials can lead to a significant increase of strength [28]. The main goal of the present study is to evaluate the potential of the SPD-processed Ti45Nb alloy to further improve its strength by heat-treatments and to study the effect on the ductility.

2. Experimental

The initial material was a commercial Ti—45Nb (wt.%) alloy rod with a diameter of 15 mm and a mean grain size of approximately 15 μm delivered by ATI specialty alloys & components (USA). A Nb content of 44.6 ± 0.2 wt.% was verified by inductively coupled plasma-optical emission spectrometry (Thermo Scientific iCAP 6500 Duo View). The oxygen content of the as-received alloy was 0.09 wt.% as determined by carrier gas hot extraction (LECO TC-436DR). After maching the rod to a diameter of 14 mm, disks with a thickness of ~1.3 mm were cut from the rod and deformed at room temperature by HPT for 5 rotations with a rotational speed of 0.6 rot/min applying a pressure of about 2.5 GPa. More details about HPT in general and the used quasi-constrained HPT setup can be found elsewhere [29,30]. The maximum von Mises strain at a radius of 7 mm after 5 rotations corresponds to a value of ~ 120. For comparative purposes one of the disks was cold-rolled from an initial thickness of ~1.7 mm down to ~0.9 mm, which corresponds to a deformation degree in terms of thickness reduction of about 0.6. Additional samples were HPT deformed at different temperatures from −196 °C (in liquid nitrogen) up to 400 °C under the same conditions as outlined above.

Subsequent isothermal and isochronal heat treatments of the at room temperature deformed material were performed to investigate the effect of annealing on the mechanical properties. The isochronal heat treatments were carried out for annealing times of 30 min in the temperature range between 100 °C and 500 °C. The isothermal heat treatments were performed at the temperature at which the isochronal treatments exhibited the hardness maximum. These isothermal heat treatments were varied between 5 min and 10 h.

The microstructural investigations were carried out on a JEOL 2100F image side C_S-corrected transmission electron microscope (TEM) with an acceleration voltage of 200 kV. The diffraction patterns were recorded on a Phillips CM 12 microscope with an acceleration voltage of 120 kV. EDX mappings were performed on a JEOL JEM-2200FS microscope with 200 kV acceleration voltage in scanning mode, equipped with an EDX system. The preparation of the TEM samples followed the conventional route of grinding, dimpling and Ar-ion thinning.

To determine the hardness of the different material states a Buehler MicroMet Vickers hardness tester with a load of 200 gf was used. For the measurements the samples were mechanically ground and polished. To account for possible changes of the Young's modulus nanoindentation experiments were performed with a diamond Berkovich indenter tip (Synton-MDP AG) on a platform Nanoindenter G200 (KLA formerly Keysight Tec) measuring the reduced modulus. Details of the measuring procedure can be found in a preceding publication [31].

In addition, the Young's modulus (E) and the Poisson's ratio (ν) were determined using Resonant Ultrasound Spectroscopy (RUS) before and after HPT processing, as well as after HPT processing and annealing. For the undeformed material state a specimen with dimensions of $4.3 \times 3.5 \times 3$ mm³ was prepared from the center of the 14 mm rod, as shown in Fig. 1a. Due to the required dimensions for RUS, another type of HPT sample with a diameter of 30 mm and a thickness of ~7 mm was used and deformed under the same conditions as the smaller HPT disks. Afterwards, prismatic specimens of the dimensions $15 \times 3.5 \times 3$ mm³ were cut in torsion direction from this specific HPT disk, see Fig. 1b. The specimens were placed between two piezoelectric transducers, one exciting vibrations, the other detecting resonances. An Agilent ENA series network analyzer with a signal-to-noise ratio of up to −140 dBm was used for signal acquisition. By calculating the resonance frequencies and minimizing the difference between experimental and theoretical ones for specific elastic parameters, the elastic constants could be obtained. This method allows determining the full tensor of elastic constants for isotropic and anisotropic materials with only one measurement. A detailed description can be found in the literature [32,33]

X-ray diffractometry (XRD) with Cu-K_α radiation was performed using a Rigaku SmartLab 5-circle diffractometer for phase analysis of the samples. Tensile tests were conducted on a Kammrath & Weiss tensile module with a loading rate of 2 μm/s equipped with a 2 kN load cell. The samples had a round cross-section with a nominal diameter of 0.5 mm and a gauge length of 2.5 mm and were produced on a specially designed grinding and polishing tool for miniaturized tensile samples [34,35]. Since the displacement could not directly be measured on the sample surface, the engineering stress is plotted against the displacement of the stroke. From this value a fracture strain was estimated by dividing the displacement of the stroke by the nominal length of the sample. Fractography of the fracture surfaces of the tensile samples
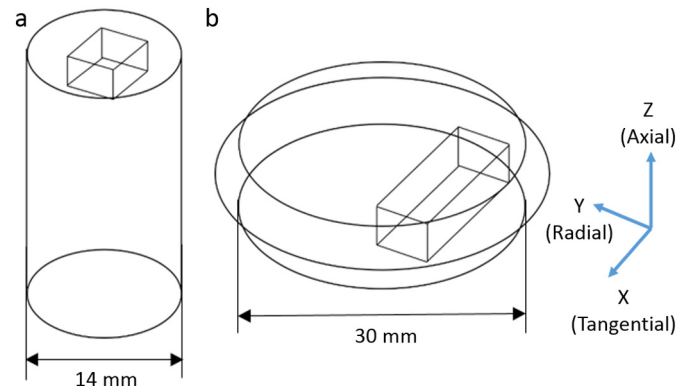

Fig. 1. Orientation of the RUS specimens within the HPT disk (right) and the rod (left) and the used coordinate system.

and further microstructural investigations were carried out on a Zeiss Auriga Dual Beam FIB/SEM equipped with a back-scatter electron (BSE) detector.

3. Results

3.1. Influence of annealing on hardness and Young's modulus

In Fig. 2a the hardness distribution along the radius of the RT-deformed sample is presented and directly compared to the hardness of the as-received material and the specimen subjected to cold rolling. Focusing on the HPT results, the hardness shows a minimum at the disk center and increases gradually along the radius until a plateau is reached. The plateau, starting at a radius of ~2 mm, is a result of reaching a minimum grain size, which remains constant after exceeding a critical deformation strain. This saturation behavior in hardness and microstructure has been thoroughly discussed in an earlier publication [36]. It is obvious that HPT deformation increases the hardness of the disks significantly. This hardness enhancement corresponds well to values obtained in earlier investigations on the same alloy [9,13]. The hardness increase after cold rolling is significantly less pronounced. The saturation hardness values of the HPT experiments performed at different deformation temperatures are presented in Fig. 2b. It is obvious that for liquid-N_2 and room temperature conditions only small differences in hardness are present. The sample deformed at 200 °C exhibits a distinct increase in saturation hardness. The maximum saturation hardness is found between 200 °C and 300 °C.

Significant microstructural states regarding Fig. 2a are presented in Fig. 3. The as-received material, Fig. 3a, has an equiaxed coarse-grained structure with an average grain size of around 15 μm. The inspection direction is parallel to the long axis of the rod material and exhibits a pronounced ⟨110⟩-fibre texture with respect to the axial direction of the subsequent HPT deformation. In Fig. 3b a BSE image of the microstructure of the cold-rolled material along the transverse direction is shown. Compared to the fully recrystallized pre-material strong contrast variations are visible, which are caused by the formation of cell structures leading to a distinct hardness increase (cf. Fig. 2a). Nevertheless, a much stronger hardness rise and a more severe refinement of the microstructure are provided by HPT-processing as presented in Fig. 3c. Using BSE-imaging only qualitative insight into the microstructure is granted. The subsequent TEM-investigations (shown later in the text) illustrate a quite homogeneous structure with grains well below 100 nm.

Post-deformation annealing experiments were exclusively performed for material deformed at room-temperature. Isochronal heat treatments (30 min), Fig. 4a, of the HPT deformed samples show a

further hardness rise up to a maximum at ~300 °C. At higher temperatures the hardness decreases again. This hardness variation reflects a similar trend as the one found for the saturation hardness for different deformation temperatures (Fig. 2b).

Along with the variation of the hardness also changes of the elastic properties were found, Fig. 4b. For the as-received state a value of ~92 GPa was measured. In the as-deformed state this value is significantly lower and increases again upon annealing up to temperatures of 400 °C. For higher temperatures the modulus declines again. To explore the kinetics of the hardening phenomenon isothermal heat treatments at the maximum hardness of 300 °C up to 10 h were carried out, Fig. 4c. The anneals at 300 °C exhibited a continuous increase in hardness up to 10 h indicating that the isochronal treatments carried out at much shorter times (30 min) do not represent an equilibrium condition. Longer annealing times were not investigated since the hardness seems to saturate. Finally also the change of the reduced modulus, E_r, of the isothermally annealed specimens was measured, Fig. 4d. Akin to the hardness, the reduced modulus increases during annealing at 300 °C and seems to saturate for very long annealing times.

3.2. Microstructural changes upon annealing

To investigate the structural changes BSE-images of selected annealing states are shown in Fig. 5b-g and compared with the HPT-state, Fig. 5a. For the isochronal anneals (upper row) the occurrence of a second phase represented by black areas can be observed. Due to the relatively low adjusted gain of the BSE detector these areas are due to mass contrast. The volume fractions estimated from digital image processing (ImageJ) are inserted in the respective images. The volume fraction of the additional phase increases markedly between 300 °C and 400 °C and decreases again at 500 °C (Figs. 5b-d). Simultaneously, at these temperatures a certain coarsening of the matrix occurs. The relative change of the volume fractions of this phase correlates to the variation of the reduced modulus with an increasing tendency up to 400 °C before it decreases at higher temperatures, see Fig. 4b. It is interesting to note that between the HPT-deformed state and the specimens subjected to 300 °C for 30 min, showing the highest hardness in the isochronal experiment, no specific change of grain size is visible. The isothermal experiments also display an increase of the volume fraction of the second phase, which again correlates to the steady rise of the reduced modulus, see Fig. 4d. Due to the low annealing temperature there is no pronounced coarsening of the matrix but a steady increase of hardness with increasing annealing time (Fig. 4c).

XRD measurements for selected isochronal (Fig. 6a) and isothermal (Fig. 6b) experiments were used to identify the newly formed phase. Comparing the HPT state with the specimens annealed at 300 °C for
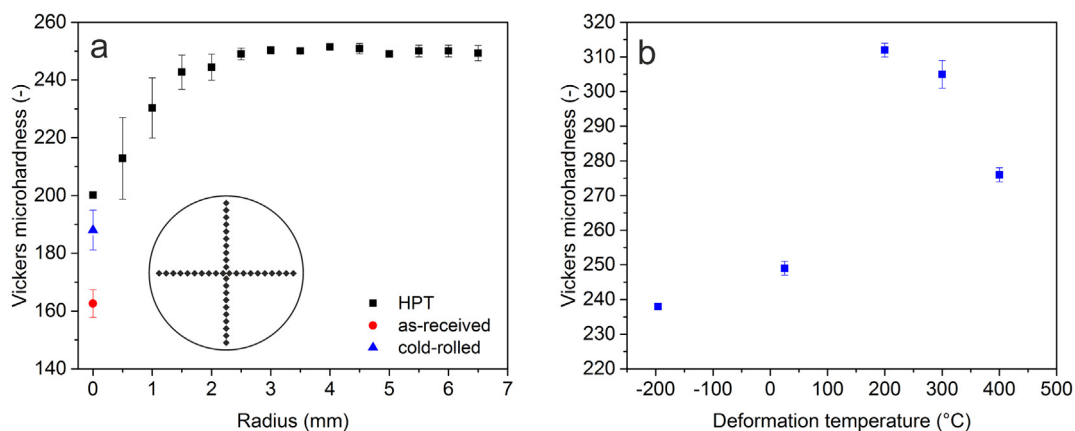

Fig. 2. Overview of the hardness measurements. (a) Average hardness of the HPT disk along the radius. The hardness was measured from the center (0 mm) to the edge of the sample (~6.5 mm). The inset shows the position of the indents on the sample surface. At a radius of about 2 mm the hardness starts to level-off into a plateau. (b) Variation of the saturation hardness for different deformation temperatures. For each value the average hardness in the plateau regime between 2 and 6.5 mm was taken.
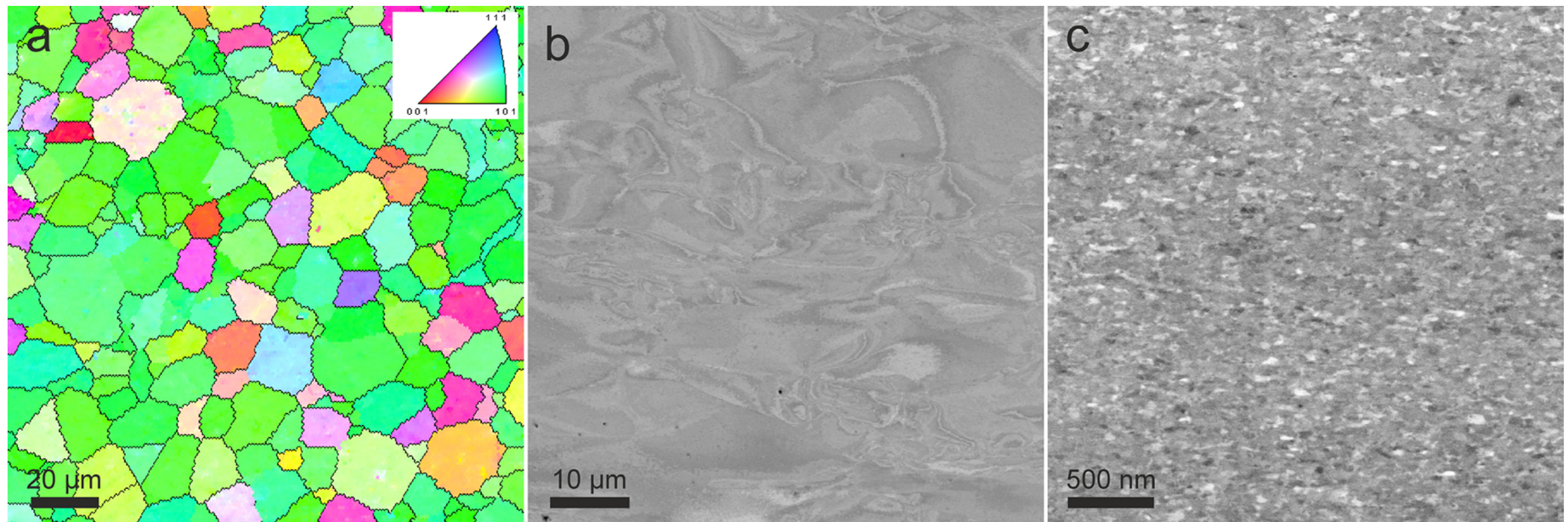
Fig. 3. Comparison between as-received (a), cold-rolled (b) and HPT-deformed (c) microstructure. The as-received state is shown with an inverse pole figure map, whereas the other two states are presented by SEM-BSE images.
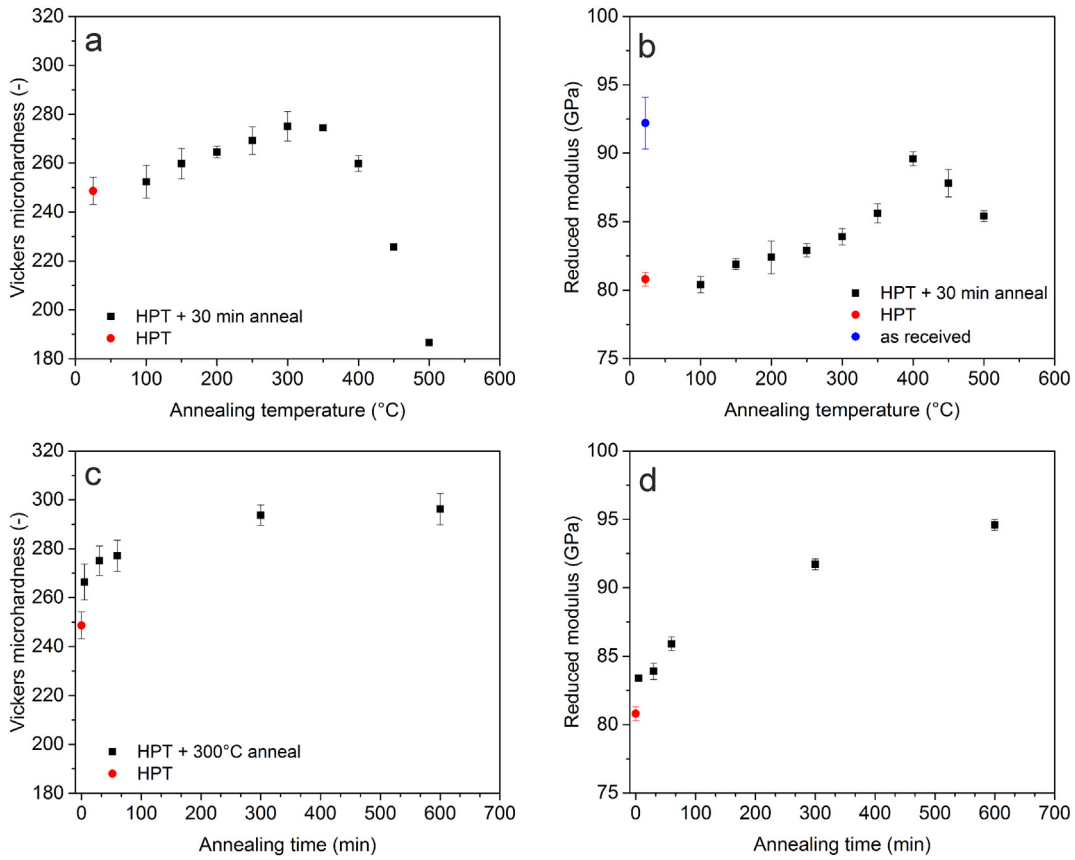
Fig. 4. Overview of the annealing experiments. Vickers microhardness (a) and reduced modulus, E_r, measurements (b) of samples that were isochronally heat-treated for 30 min. The hardness has a maximum at approximately 300 °C, whereas E_r increases up to 400 °C. Vickers hardness measurements (c) and E_r measurements (d) after isothermal heat treatments carried out at 300 °C for up to 10 h. With rising annealing time hardness and reduced modulus steadily increase.
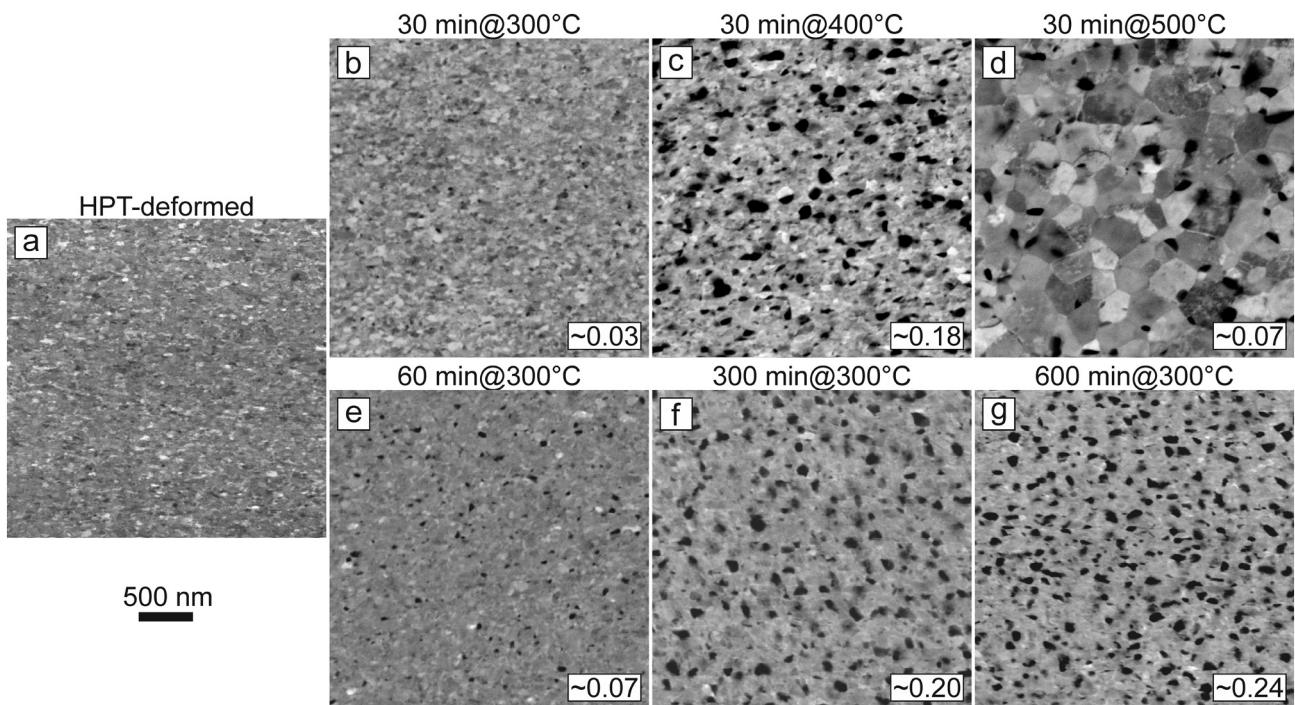

Fig. 5. Microstructural changes of HPT-deformed Ti45Nb upon annealing. The initial material for the heat treatments was the HPT-deformed material (a). In the upper row microstructures after 30 min at 300 °C (b), 400 °C (c) and 500 °C (d) are shown. In the lower row isothermally annealed microstructures at 300 °C for 60 min (e), 300 min (f) and 600 min (g) are presented.
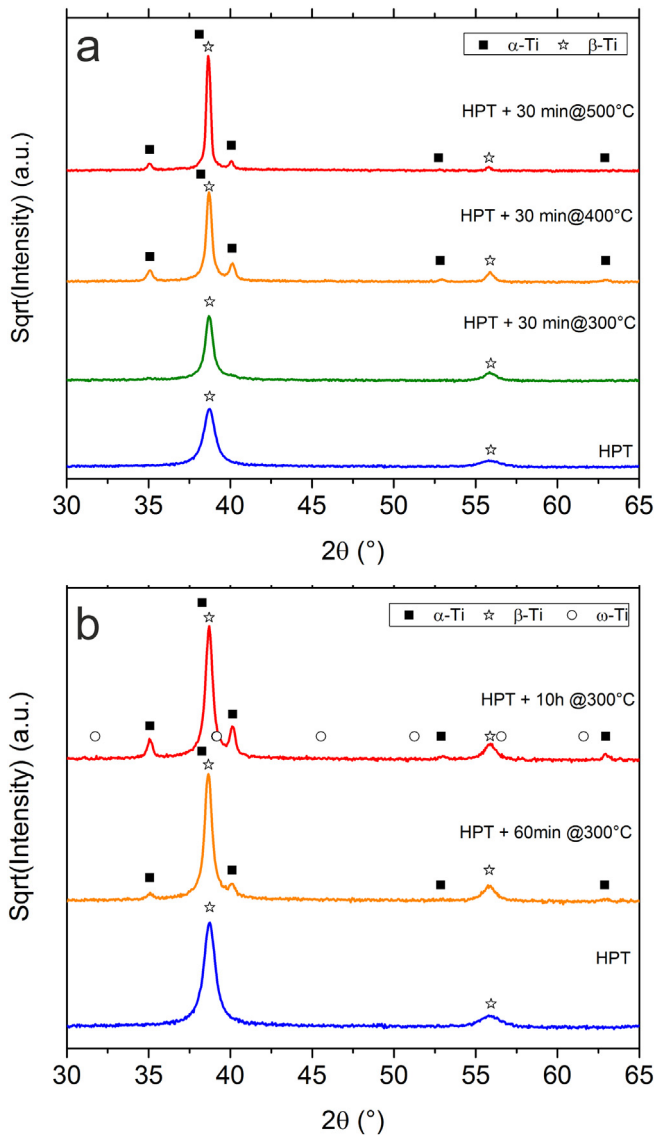
Fig. 6. XRD diffraction patterns of HPT-deformed Ti45Nb after isochronal (a) and isothermal (b) heat treatments.

30 min (Fig. 6a) no distinct change of the reflexes is visible except for a small decrease of the peak width and only the β-phase is present. Annealing at 400 °C leads to the occurrence of additional peaks, which fit well to α-Ti. Compared to the β-phase their intensity is rather small but still significant. The missing peaks for 300 °C can be most likely explained by the relatively small volume fraction of the additional phase and its small crystal size leading to tiny, heavily broadened Bragg peaks that are beyond the resolution limit. For the specimens annealed at 500 °C the intensity of the α-Ti peaks and thus the volume fraction of α-Ti decreases again. This tendency correlates well with the findings deduced from the BSE images and the trend of the modulus change (Fig. 4b). In the isothermal case, Fig. 6b, the intensity of the peaks of the additional phase steadily increases, which corresponds to the microstructural findings in Figs. 5e–g and the continuous increase of the reduced modulus (Fig. 4d). For comparative purposes also the theoretical peak-positions of ω-Ti are inserted in Fig. 6b [37], suggesting that this specific phase does not form.

Further insights into the microstructure are obtained using TEM. In Fig. 7a the microstructure of the HPT-deformed material is presented with a STEM-image. Typical of SPD microstructures the grain boundaries are difficult to discern, which is often related to internal stresses and high defect densities in the sample [38]. In Fig. 7b a corresponding

electron diffraction pattern shows the single-phase character of the microstructure. The pattern consists only of rings that can be ascribed to the bcc structure of Ti45Nb. The single-phase state is also confirmed by the high angle angular dark field (HAADF) image in Fig. 7c, which shows no large contrast variations as it would be typical for the presence of a second phase. These findings confirm the single-phase character of the material after HPT deformation, similar as it has already been reported in previous studies [9,13].

Subsequent annealing treatments of the as-deformed material change the microstructure significantly. Here, only investigations for the highest hardness increase after isothermal heat treatments, namely after 10 h at 300 °C, were performed. The STEM image in Fig. 7d indicates a clearer and more relaxed microstructure with better defined boundaries. The electron diffraction pattern (Fig. 7e) shows several discrete rings in addition to the diffraction rings of the β-matrix. These extra rings can be ascribed to a hexagonal close-packed crystal structure (α-Ti). The HAADF-image (Fig. 7f) exhibits grains with strong contrast differences compared to the matrix, implying a difference in the chemical composition of the additionally formed phase. Similar results regarding the observed mass contrast were presented before with the BSE-images (Fig. 5).

In order to get more insights into the local chemistry changes during annealing, position-resolved EDS measurements were performed for the same microstructural state as presented in Fig. 7. Fig. 8a and b show the maps of Nb (green) and Ti (red) and illustrate that these particles are depleted in Nb and enriched in Ti. Quantitative chemical data was collected with spot measurements, see Fig. 8c. The corresponding chemical compositions of the positions A-D are compiled in Table 1. In detail, spot A represents a grain with a composition, close to the initial composition with a content of 49 wt.% Nb. Spots B and D reveal the additional hexagonal phase with a significant enrichment of Ti (about 90 wt.%). The additional phase is formed at grain boundaries, as demonstrated by position D. In spot C, where a brighter area at the grain boundary was analyzed, an enrichment of Nb to about 67 wt.% compared to the initial alloy composition (equivalent to a depletion in Ti) was measured. Due to the large chemical variations found at grain boundary regions (spots C and D) one can conclude that the phase formation occurs predominantly at grain boundaries and triple junctions, which are known for enhanced diffusivity and for being preferential nucleation sites for phase formation.

The electron diffraction experiments showing reflexes corresponding to a hcp-phase and the EDS measurements, which indicate that the newly formed phase is enriched in Ti, lead to the result that during the heat treatments performed in this study a hexagonal phase mainly containing Ti, is formed. A comparison of the results with the Ti—Nb phase diagram proves that the crystal structure of the additional phase corresponds to the Ti-rich α-Ti equilibrium phase existing at temperatures below ~550 °C [39]. The thermodynamic equilibrium structure of Ti45Nb at 300 °C is an α + β two-phase structure. The single-phase β-state is a metastable state and does not represent the thermodynamic equilibrium for this alloy at room temperature. In the ultrafine-grained material the rapid formation of the α-phase can be explained due to the large amount of grain boundaries and triple junctions in HPT-deformed materials, which represent preferential nucleation sites and fast diffusion pathways.

3.3. Tensile behavior

Fig. 9a presents the tensile test results, and significant characteristic values including the ultimate strength, σ_{UTS}, the fracture strain, ε_{fra}, and reduction of area, Z, are summarized in Table 2. From the heat-treated states only measurements of specimens subjected to 300 °C for 10 h were made, as this state showed the largest hardness increase. For the cold-rolled specimens, the strength increases by about 115 MPa compared to the as-received material. A more pronounced change in strength is obtained after HPT deformation, revealing an increase of more than twice the strength of the as-received material after HPT. In
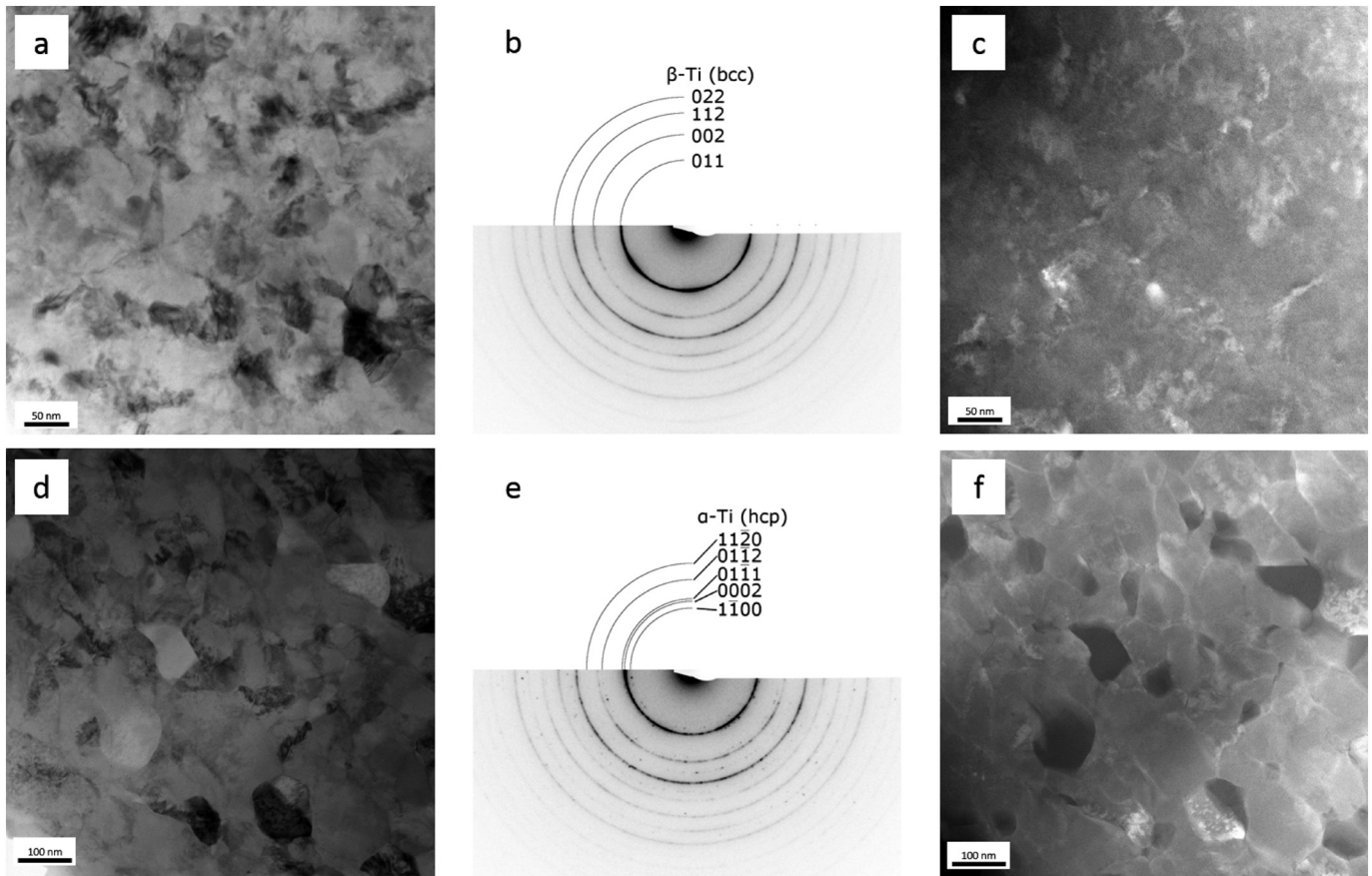
Fig. 7. Microstructural investigations of the HPT-deformed sample (a–c) and the heat-treated state after annealing for 10 h at 300 °C (d–f). (a and d represent bright-field scanning transmission electron microscope (STEM) images, b and e selected area diffraction images, c and f high angle annular dark-field (HAADF) micrographs). The HPT-deformed state is purely bcc single-phased (a–c). For the heat-treated state an additional hexagonal close-packed (hcp) α-Ti phase was identified by indexing the SAD pattern (e). An additional hint for phase formation is given by the strong contrast changes in the HAADF image (f).

comparison with the cold-rolled state, HPT deformation does not seem to affect the ductility significantly, even though the tensile strength is significantly enhanced. Subsequent annealing treatments of the HPT-deformed samples at 300 °C for 10 h increased the strength further, up to about 1200 MPa, which is almost three times the strength of the initial coarse-grained material. The strength enhancement is however partly compensated by a decrease in ductility, when ε_{fra} and Z in Table 2 are reviewed.

The fractographic images shown in Fig. 9b present the ductility of the material states of Fig. 9a by the residual macroscopic fracture surfaces, which were also used to calculate the reduction of area. It is obvious that the as-received state exhibits the strongest necking followed by the cold-rolled sample. After HPT processing the macroscopic ductility further decreases and for the heat-treated state the residual fracture surface is the largest, which implies that the ductility in terms of area reduction is further reduced by the heat treatment.
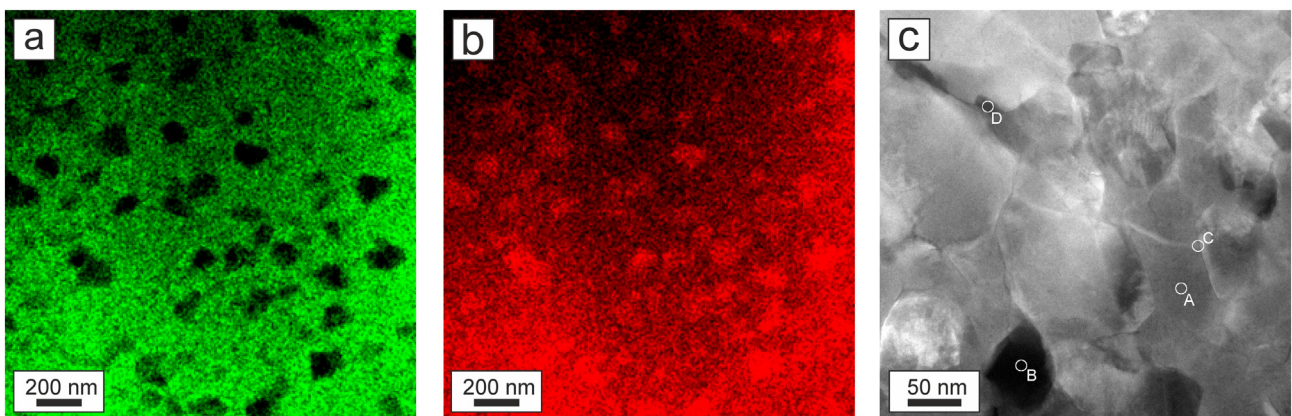

Fig. 8. Chemical analysis of the HPT-deformed and subsequently at 300 °C for 10 h annealed sample performed with EDS. EDS maps of Nb (a) and Ti (b) showing that the second phase particles are depleted in Nb and enriched in Ti. (c) HAADF image of the structure. The letters A – D indicate the positions of EDS-spot measurements. The compositions can be found in Table 1.

Table 1
Chemical compositions according to the EDS-spot measurements at positions A-D as indicated in Fig. 7c. The error of the results is in the order of ±0.1 wt.%.

Spot	Ti (wt.%)	Nb (wt.%)
A	51	49
B	94	6
C	33	67
D	88	12

Table 2
Summary of the tensile tests with ultimate strength, σ_{UTS}, maximum displacement of the stroke before fracture, $disp_{max}$, fracture strain, ε_{fra}, and reduction of area, Z.

Material-state	Sample	σ_{UTS} (MPa)	$displ_{max}$ (μm)	ε_{fr} (%) (%)	Z (%) (%)
As-received	1	450	470	18.8	97
	2	430	500	20	97
Cold-rolled	1	550	350	14	85
	2	560	350	14	85
HPT-deformed	1	990	380	15.2	66
	2	990	340	13.6	71
Annealed@300 °C/10 h	1	1200	160	6.4	23
	2	1215	200	8	35

4. Discussion

The possibility to increase the tensile strength of Ti45Nb by HPT deformation through grain refinement has already been presented and discussed in earlier studies [9,12,13]. In the focus of the present study was the annealing behavior of the material. It could be shown that the alloy possesses good thermal stability up to 300 °C. The thermal stability is accompanied by an additional strength increase, which could be used to further enhance the strength of the alloy and of components manufactured from the SPD-processed alloy.

4.1. Effect of annealing on hardness

A hardness increase upon annealing is a frequently examined phenomenon in ultrafine-grained and nanocrystalline materials. The origin of the hardening upon annealing is however not fully understood. On one hand, the hardening could be attributed to a decrease in the defect density upon annealing [28,40]. This is qualitatively confirmed by the TEM images showing a clearer microstructure and better discernable boundaries after annealing. In addition, a slight decrease in the width of the peaks in the XRD measurements is visible, for example when comparing the HPT material to the annealed state at 300 °C for 30 min. It is suggested that when mobile dislocations are annealed out, grain boundary sources have to be activated and for that higher stress levels are required than for the movement of mobile dislocations in the grain interior.

On the other hand, segregates or second phases at grain boundaries are considered to increase the strength upon annealing [41]. In the annealed specimens a second phase was found, as shown above. Decomposition along the grain boundaries was revealed by STEM, where some grain boundaries were found to be brighter than others. EDS investigations of such brighter grain boundaries revealed that they are somewhat enriched in Nb and the darker precipitates are enriched in Ti. The second phase can hinder dislocation emission from or relaxation of dislocations at the grain boundaries. The particles of the new phase, however, seem to be quite large and it is debatable if they are effective for hindering dislocation emission from the grain boundaries. Nevertheless, it is also possible that smaller precipitates, which are more difficult to detect, control the hardening response.

The classical strengthening effect caused by second phases, known from precipitation hardening, can be ruled out since the second phase is exclusively retrievable as an individual phase adjacent to β-phase grains. To be an efficient obstacle for dislocation motion these precipitates would be required to be located in the grain interior. Except for being obstacles for dislocation motion, large volume fractions of a second phase can also constrain the deformation of a composite structure, which also leads to an increase of strength. Such a hardening mechanism is typical for duplex-steels and was also found to be relevant for nanocrystalline alloys consisting of various intermetallic phases that constrain the deformation of a relatively soft face-centered cubic matrix phase [30]. In such a case the composite formation consisting of phases with different contributions to the strength is the key feature for the hardness increase.

Even though there are different conceivable considerations explaining the hardness increase in such nanocrystalline alloys, a clear answer to this question cannot be given on the basis of our observations. On one hand, the microstructure after 30 min at 300 °C showing the maximum hardness in the isochronal annealing treatments has only a
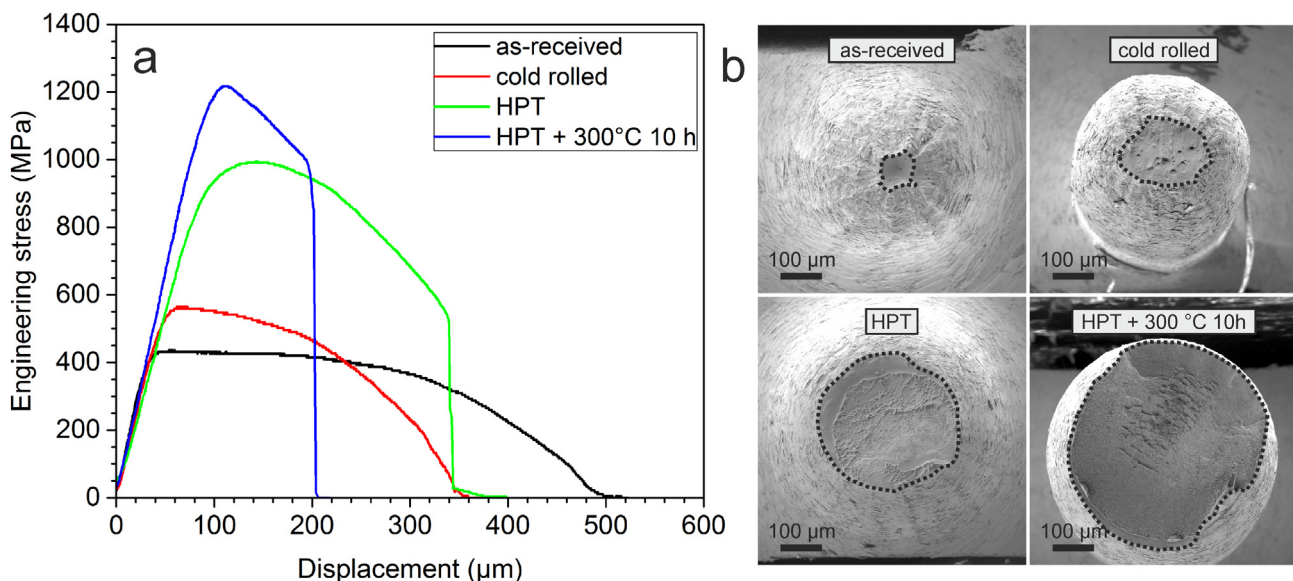

Fig. 9. Tensile experiments performed on various microstructural states of Ti45Nb. a) The as-received, cold-rolled, HPT-deformed and an annealed HPT sample (300 °C for 10 h) are compared. b) Typical fractographs of the tensile samples at low magnifications. Dotted lines are inserted to improve the visibility of the residual fracture surface.

very small second phase volume fraction at this early stage of annealing. This questions the significance of the second phases for the hardness increase. Controversial to that, for longer annealing times at the same temperature the hardness further increases, together with a growth of the volume fraction of the additional phase. This observation and the large volume fractions for long annealing times favors the importance of the second phase for the hardness increase caused by the composite formation. Therefore, it seems that both, defect annihilation and composite formation, control the hardness increase, whereby the hardening due to defect annihilation is prevalent at the early stages of annealing (short annealing times) and hardening due to composite formation is significant in the later stages (long annealing times).

4.2. Effect of annealing on elastic properties

The results show that the elastic properties are affected by HPT processing and annealing as well. As a main measure for the elastic properties the reduced modulus provided by nanoindentation was used, as it allows to investigate very small sample quantities. The value before HPT-processing using the nanoindentation approach- is ~92 GPa and drops down to about 81 GPa after deformation. The strong variation of the Young's modulus of this type of alloy with the crystallographic direction [42] paired with a distinctive change of the texture between the undeformed and deformed state is a possible explanation for this behavior. The increase of the modulus during the heat treatments seems to be caused by the formation of α titanium, which has a Young's modulus of ~111 GPa [43].

The results of RUS measurements of selected material states are shown in Table 3. For all material states, a distinctive anisotropy of the elastic constants is observed. For the undeformed sample, a value of 61.3 GPa for E_z and in-plane values ($E_x = E_y$) of 72.0 GPa were measured assuming a transversally isotropic material behavior. For an isotropic polycrystalline sample, a value of 65.5 GPa would be expected [42]. The Poisson ratio reflects the anisotropy as well. The origin of the anisotropy may be related to the strong texture of the initial material, see Fig. 3a. After deformation, similar to the trend found using nanoindentation, E_x and E_y slightly drops whereas E_z increases. Since it was proven that no additional phase formation occurs between the as-received and HPT-deformed state, the change in the elastic constants can be ascribed to the change of the texture between the undeformed and the HPT-deformed material. As a third RUS experiment one sample was heat-treated at 300 °C for 10 h, introducing the largest change of the elastic behavior in the nanoindentation experiments. An increase in the moduli values (E_z, $E_x = E_y$) was found, showing that both techniques, nanoindentation and RUS, are capable of reflecting the increase of the modulus upon annealing. The reason for the increase seems to be the increasing α titanium content. For several applications as an implant material this slight increase of the modulus is disadvantageous so that future work may concentrate on finding the optimum between additional strengthening and changes of the elastic properties.

Taking the measured elastic constants of the material after high pressure torsion and for pure hcp-Ti a typical value of 111 GPa [43], the expected elastic constants for the heat-treated states are calculated using a simple rule of mixtures. The measured volume fraction after annealing for 10 h at 300 °C is approximately 24 vol%, which would yield a Young's modulus of 80.2 GPa for $E_x = E_y$ and 77.9 GPa for E_z. Regarding E_x and E_y the result is close to the measured value of 79.0 GPa,

suggesting that the change of Young's modulus is mainly controlled by the α-precipitation. However, the calculated and measured E_z values show a distinctive discrepancy (see again Table 3). The origin for this difference could be twofold. At first, grain growth during annealing could lead to a change in texture and dominate the change of the Young's modulus rather than the α-precipitation. However, SEM images (Fig. 5e–g) and the comparison of the TEM images of the HPT-processed state and the annealed state (Fig. 7a and d) suggest no grain growth. It is more likely that the α-phase is distributed in a specific geometrical arrangement in the β-matrix. It is well-known that HPT-deformed structures often exhibit elongated grains with a certain aspect ratio when inspected along the radial direction [36]. The grain shape in combination with preferential precipitation at triple junctions could lead to a directional dependence of the additional stiffening of the β-matrix -as suggested by the RUS measurements- and could be the reason why a simple rule of mixtures is not applicable for all directions.

4.3. Impact of annealing on ductility

Besides the strength and the elastic properties the ductility of the material is also influenced by the microstructural state. In comparison with the as-received and recrystallized state, the HPT-deformed material exhibits a decrease of ductility. However, the recrystallized state with its low strength is of rather low relevance for an application-oriented comparison. A better comparison is given by the cold-rolled state, which is closer to industrial needs. The cold-rolled material exhibits a similar ductility as the HPT state, but the HPT deformation leads to considerably higher strength. Even though the further enhancement of strength by the heat treatment leads to a reduction of ductility compared to HPT processing without annealing, a substantial amount of ductility remains as the specimen shows necking before failure.

In order to learn more about the failure behavior of the different material states fractographic images taken at higher magnifications are provided in Fig. 10. The undeformed state, Fig. 10a, displays ductile failure with only few large dimples due to the high purity of the material resulting in only few inclusions being activated for void nucleation. By increasing the strength, smaller inclusions become relevant for void initiation and the void density increases, as shown for the cold-rolled state (Fig. 10b). For the HPT state, Fig. 10c, still micro-ductile fracture features can be found. In contrast to the as-received and cold-rolled material the dimple features however have changed markedly. In the coarse-grained regime (as-received and cold-rolled) the dimples are mainly initiated at second phase particles, i.e. inclusions. For the nanocrystalline state, the size of the dimples markedly decreases and the voids seem not to be initiated from inclusions any longer. Instead, triple junctions and grain boundaries are suggested to be the initiation sites for void nucleation [44]. This is also confirmed by the fractographic observations, Fig. 10c, which prove that the void diameter is much larger than the grain size (compare Fig. 7 with Fig. 10c). The heat treatment, Fig. 10d, causes a pronounced change of the fractographic features. Again, micro-dimples are visible with somewhat smaller diameters, which could be related to the decrease in ductility between the HPT-deformed and heat-treated state. Second phase particles could however not be found on the fracture surfaces so that their influence on the deterioration of ductility seems to be negligible.

5. Summary

In this investigation it was shown that the strength of the Ti45Nb alloy deformed by HPT can be significantly increased by subsequent heat treatment. The strength increase due to annealing also leads to a change in the elastic properties exhibiting a pronounced anisotropy. Microstructural investigations using TEM revealed the formation of a Ti-rich α-phase at grain boundaries. Even though the increase of the Young's modulus seems to be caused by the second phase particles, their role for the hardness increase and their effect on the ductility is

Table 3
Elastic constants as obtained by RUS. The measures have a typical uncertainty of ±1.5 GPa for E and ± 0.02 for ν.

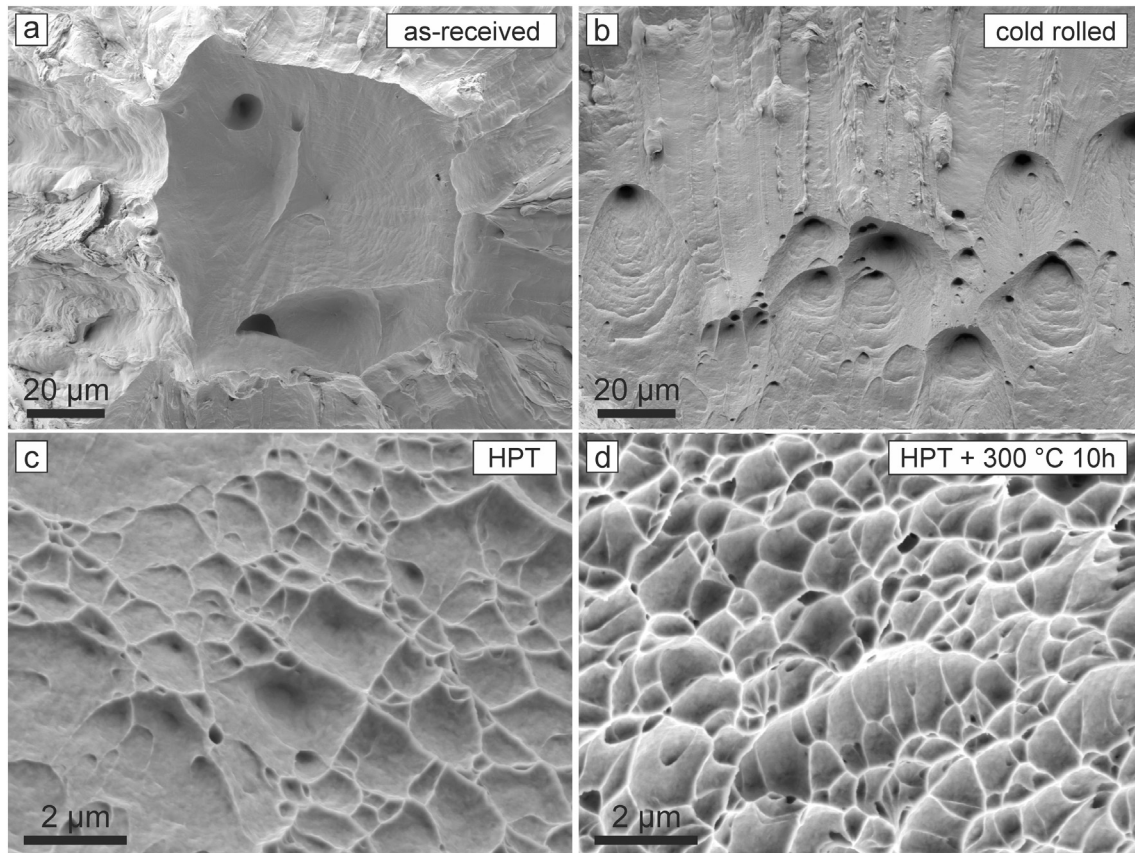| Material state	$E_x = E_y$ (GPa)	E_z (GPa)	$\nu_{yz} = \nu_{xz}$	ν_{xy}
As-received	72.0	61.3	0.267	0.312
HPT	70.5	67.4	0.326	0.436
HPT + 300 °C	79.0	70.1	0.299	0.351

Fig. 10. Typical fractographs of the tensile samples at high magnifications showing the prevalence of ductile fracture independent of the microstructural state.

not fully clear. To conclude, heat treatments are a promising strategy to further increase the strength of nanostructured biocompatible alloys for load bearing applications.

Data availability statement

The raw/processed data required to reproduce these findings cannot be shared at this time as the data also forms part of an ongoing study.

CRediT authorship contribution statement

B. Völker: Investigation, Formal analysis, Writing. **V. Maier-Kiener:** Investigation, Formal Analysis, Writing. **K. Werbach;** Investigation, Formal Analysis, Writing. **T. Müller:** Investigation, Formal Analysis, Scientific discussion. **S. Pilz:** Material, Scientific discussion. **M. Calin:** Scientific discussion. **J. Eckert:** Scientific discussion. **A. Hohenwarter** Investigation, Formal analysis, Writing.

Declaration of Competing Interest

There are no conflicts to declare.

Acknowledgements

References

[1] S.G. Fedotov, P.K. Belousov, Elastic constants of the system titanium-niobium, Fiz. Met. Met. 17 (1964) 83–86.
[2] S. Hanada, T. Ozaki, E. Takahashi, S. Watanabe, K. Yoshimi, T. Abumiya, Composition dependence of young's modulus in beta titanium binary alloys, Mat. Sci. Forum 426-432 (2003) 3103–3108, https://doi.org/10.4028/www.scientific.net/MSF.426-432.3103.
[3] T. Ozaki, H. Matsumoto, S. Watanabe, S. Hanada, Beta Ti alloys with low Young's modulus, Mater. Trans. 45 (2004) 2776–2779, https://doi.org/10.2320/matertrans.45.2776.
[4] M. Long, H.J. Rack, Titanium alloys in total joint replacement—a materials science perspective, Biomaterials 19 (1998) 1621–1639, https://doi.org/10.1016/S0142-9612(97)00146-4.
[5] M. Niinomi, Mechanical properties of biomedical titanium alloys, Mater. Sci. Eng. A 243 (1998) 231–236, https://doi.org/10.1016/S0921-5093(97)00806-X.
[6] M. Niinomi, T. Hattori, K. Morikawa, T. Kasuga, A. Suzuki, H. Fukui, et al., Development of low rigidity beta-type titanium alloy for biomedical applications, Mater. Trans. 43 (2002) 2970–2977, https://doi.org/10.2320/matertrans.43.2970.
[7] M. Niinomi, M. Nakai, Titanium-based biomaterials for preventing stress shielding between implant devices and bone, Int. J. Biomater. (2011), 836587. https://doi.org/10.1155/2011/836587.
[8] H. Yilmazer, M. Niinomi, M. Nakai, K. Cho, J. Hieda, Y. Todaka, et al., Mechanical properties of a medical β-type titanium alloy with specific microstructural evolution through high-pressure torsion, Mater. Sci. Eng. C 33 (2013) 2499–2507, https://doi.org/10.1016/j.msec.2013.01.056.
[9] A. Panigrahi, B. Sulkowski, T. Waitz, K. Ozaltin, W. Chrominski, A. Pukenas, et al., Mechanical properties, structural and texture evolution of biocompatible Ti–45Nb alloy processed by severe plastic deformation, J. Mech. Behav. Biomed. Mater. 62 (2016) 93–105, https://doi.org/10.1016/j.jmbbm.2016.04.042.
[10] Y.C. Wang, T.G. Langdon, Effect of heat treatment on microstructure and microhardness evolution in a Ti–6Al–4V alloy processed by high-pressure torsion, J. Mater. Sci. 48 (2013) 4646–4652, https://doi.org/10.1007/s10853-012-7071-1.
[11] M. Geetha, A.K. Singh, K. Muraleedharan, A.K. Gogia, R. Asokamani, Effect of thermomechanical processing on microstructure of a Ti–13Nb–13Zr alloy, J. Alloys Compd. 329 (2001) 264–271, https://doi.org/10.1016/S0925-8388(01)01604-8.

[12] R.Z. Valiev, Y. Estrin, Z. Horita, T.G. Langdon, M.J. Zehetbauer, Y.T. Zhu, Fundamentals of superior properties in bulk nanoSPD materials, Mater. Res. Lett. 4 (2016) 1–21, https://doi.org/10.1080/21663831.2015.1060543.

[13] B. Völker, N. Jäger, M. Calin, M. Zehetbauer, J. Eckert, A. Hohenwarter, Influence of testing orientation on mechanical properties of Ti45Nb deformed by high pressure torsion, Mater. Des. 114 (2017) 40–46, https://doi.org/10.1016/j.matdes.2016.10.035.

[14] A. Helth, S. Pilz, T. Kirsten, L. Giebeler, J. Freudenberger, M. Calin, et al., Effect of thermomechanical processing on the mechanical biofunctionality of a low modulus Ti-40Nb alloy, J. Mech. Behav. Biomed. Mater. 65 (2017) 137–150, https://doi.org/10.1016/j.jmbbm.2016.08.017.

[15] S. Pilz, D. Geissler, M. Calin, J. Eckert, M. Zimmermann, J. Freudenberger, et al., Thermomechanical processing of In-containing β-type Ti-Nb alloys, J. Mech. Behav. Biomed. Mater. 79 (2018) 283–291, https://doi.org/10.1016/j.jmbbm.2017.12.028.

[16] A.P. Zhilyaev, G.V. Nurislamova, B.-K. Kim, M.D. Baró, J.A. Szpunar, T.G. Langdon, Experimental parameters influencing grain refinement and microstructural evolution during high-pressure torsion, Acta Mater. 51 (2003) 753–765, https://doi.org/10.1016/S1359-6454(02)00466-4.

[17] R. Valiev, Nanostructuring of metals by severe plastic deformation for advanced properties, Nat. Mater. 3 (2004) 511–516, https://doi.org/10.1038/nmat1180.

[18] R.Z. Valiev, Y. Estrin, Z. Horita, T.G. Langdon, M.J. Zechetbauer, Y.T. Zhu, Producing bulk ultrafine-grained materials by severe plastic deformation, JOM 58 (2006) 33–39, https://doi.org/10.1007/s11837-006-0213-7.

[19] R. Pippan, F. Wetscher, M. Hafok, A. Vorhauer, I. Sabirov, The limits of refinement by severe plastic deformation, Adv. Eng. Mat. 8 (2006) 1046–1056, https://doi.org/10.1002/adem.200600133.

[20] A. Vorhauer, R. Pippan, On the homogeneity of deformation by high pressure torsion, Scr. Mater. 51 (2004) 921–925, https://doi.org/10.1016/j.scriptamat.2004.04.025.

[21] A.P. Zhilyaev, T.G. Langdon, Using high-pressure torsion for metal processing: fundamentals and applications, Prog. Mater. Sci. 53 (2008) 893–979, https://doi.org/10.1016/j.pmatsci.2008.03.002.

[22] A. Hohenwarter, A. Bachmaier, B. Gludovatz, S. Scheriau, R. Pippan, Technical parameters affecting grain refinement by high pressure torsion, Int. J. Mater. Res. 100 (2009) 1653–1661, https://doi.org/10.3139/146.110224.

[23] R.K. Islamgaliev, V.U. Kazyhanov, L.O. Shestakova, A.V. Sharafutdinov, R.Z. Valiev, Microstructure and mechanical properties of titanium (grade 4) processed by high-pressure torsion, Mater. Sci. Eng. A 493 (2008) 190–194, https://doi.org/10.1016/j.msea.2007.08.084.

[24] I. Sabirov, R.Z. Valiev, I.P. Semenova, R. Pippan, Effect of equal channel angular pressing on the fracture behavior of commercially pure titanium, Metall. Mater. Trans. A. 41 (2010) 727–733, https://doi.org/10.1007/s11661-009-0111-z.

[25] Y. Estrin, H.-E. Kim, R. Lapovok, H.P. Ng, J.-H. Jo, Mechanical strength and biocompatibility of ultrafine-grained commercial purity titanium, Biomed. Res. Int. (2013), 914764. https://doi.org/10.1155/2013/914764.

[26] I. Sabirov, R.Z. Valiev, R. Pippan, About application of three dimensional analyses of fracture surfaces in fracture study on nanostructured titanium, Comput. Mater. Sci. 76 (2013) 72–79, https://doi.org/10.1016/j.commatsci.2012.12.027.

[27] Y.M. Wang, E. Ma, Three strategies to achieve uniform tensile deformation in a nanostructured metal, Acta Mater. 52 (2004) 1699–1709, https://doi.org/10.1016/j.actamat.2003.12.022.

[28] X. Huang, N. Hansen, N. Tsuji, Hardening by annealing and softening by deformation in nanostructured metals, Science 312 (2006) 249–251, https://doi.org/10.1126/science.1124268.

[29] R. Pippan, S. Scheriau, A. Hohenwarter, M. Hafok, Advantages and limitations of HPT: A review, Mater. Sci. Forum 584-586 (2008) 16–21, https://doi.org/10.1016/j.pmatsci.2008.03.002.

[30] B. Schuh, F. Mendez-Martin, B. Völker, E.P George, H. Clemens, R. Pippan, A. Hohenwarter, Technical parameters affecting grain refinement by high pressure torsion, Acta Mater. 96 (2015) 258–268, https://doi.org/10.1016/j.actamat.2015.06.025.

[31] V. Maier-Kiener, B. Schuh, E.P. George, H. Clemens, A. Hohenwarter, Nanoindentation testing as a powerful screening tool for assessing phase stability of nanocrystalline high-entropy alloys, Mater. Des. 115 (2017) 479–485, https://doi.org/10.1016/j.matdes.2016.11.055.

[32] A. Migliori, J.L. Sarrao, W.M. Visscher, T.M. Bell, M. Lei, Z. Fisk, et al., Resonant ultrasound spectroscopic techniques for measurement of the elastic moduli of solids, Phys. B Phys. Condens. Matter. 183 (1993) 1–24, https://doi.org/10.1016/0921-4526(93)90048-B.

[33] R.G. Leisure, F.A. Willis, Resonant ultrasound spectroscopy, J. Phys. Condens. Matter. 9 (1997) 6001–6029, https://doi.org/10.1088/0953-8984/9/28/002.

[34] G.B. Rathmayr, A. Bachmaier, R. Pippan, Development of a new testing procedure for performing tensile tests on specimens with sub-millimetre dimensions, J. Test. Eval. 41 (2013) 635–646, https://doi.org/10.1520/JTE20120175.

[35] G.B. Rathmayr, A. Bachmaier, High Quality Tensile Tests on the Mesoscale, www.microsample.eu 2017 (accessed November 12, 2017).

[36] R. Pippan, S. Scheriau, A. Taylor, M. Hafok, A. Bachmaier, Saturation of fragmentation during severe plastic deformation, Annu. Rev. Mater. Res. 40 (2010) 319–343, https://doi.org/10.1146/annurev-matsci-070909-104445.

[37] E.S. Chebotareva, S.G. Nuzhdina, Observation of omega-titanium in a composite hard facing alloy based on fine-grain diamonds locality: synthetic sample: at P = 4 GPa, known as the omega phase, Fiz. Met. I Metalloved. 36 (1973) 200–202.

[38] X. Sauvage, G. Wilde, S.V. Divinski, Z. Horita, R.Z. Valiev, Grain boundaries in ultrafine grained materials processed by severe plastic deformation and related phenomena, Mater. Sci. Eng. A 540 (2012) 1–12, https://doi.org/10.1016/j.msea.2012.01.080.

[39] L. Rokhlin, N. Bochvar, T. Dobatkina, V. Tomashik, M. Materials Science International Team, Nb-Ti binary phase diagram evaluation · phase diagrams, crystallographic and thermodynamic data: datasheet from MSI Eureka in SpringerMaterials, (n.d.). https://materials.springer.com/msi/docs/sm_msi_r_20_012723_01.

[40] O. Renk, A. Hohenwarter, K. Eder, K.S. Kormout, J.M. Cairney, R. Pippan, Increasing the strength of nanocrystalline steels by annealing: is segregation necessary? Scr. Mater. 95 (2015) 27–30, https://doi.org/10.1016/j.scriptamat.2014.09.023.

[41] R.Z. Valiev, N.A. Enikeev, M.Y. Murashkin, V.U. Kazykhanov, X. Sauvage, On the origin of the extremely high strength of ultrafine-grained Al alloys produced by severe plastic deformation, Scr. Mater. 63 (2010) 949–952, https://doi.org/10.1016/j.scriptamat.2010.07.014.

[42] R. Hermann, H. Hermann, M. Calin, B. Büchner, J. Eckert, Elastic constants of single crystalline beta-Ti 70 Nb 30, 66 (2012) 198–201, https://doi.org/10.1016/j.scriptamat.2011.10.039.

[43] H.P. Stüwe, Einführung in die Werkstoffkunde, 2nd ed. B.I.-Hochschultaschenbücher, Mannheim, 1978.

[44] A. Pineau, A. Amine Benzerga, T. Pardoen, Failure of metals III: fracture and fatigue of nanostructured metallic materials, Acta Mater. 107 (2016) 508–544, https://doi.org/10.1016/j.actamat.2015.07.049.